FULL PAPER

Magnetic Resonance in Medicine 00:00–00 (2016)

Accelerated Exponential Parameterization of T2 Relaxation with Model-Driven Low Rank and Sparsity Priors (MORASA)

Xi Peng,[1,2] Leslie Ying,[3] Yuanyuan Liu,[1] Jing Yuan,[4] Xin Liu,[1,2] and Dong Liang[1,2]*

Purpose: This work is to develop a novel image reconstruction method from highly undersampled multichannel acquisition to reduce the scan time of exponential parameterization of T2 relaxation.

Theory and Methods: On top of the low-rank and joint-sparsity constraints, we propose to exploit the linear predictability of the T2 exponential decay to further improve the reconstruction of the T2-weighted images from undersampled acquisitions. Specifically, the exact rank prior (i.e., number of non-zero singular values) is adopted to enforce the spatiotemporal low rankness, while the mixed L2–L1 norm of the wavelet coefficients is used to promote joint sparsity, and the Hankel low-rank approximation is used to impose linear predictability, which integrates the exponential behavior of the temporal signal into the reconstruction process. An efficient algorithm is adopted to solve the reconstruction problem, where corresponding nonlinear filtering operations are performed to enforce corresponding priors in an iterative manner.

Results: Both simulated and in vivo datasets with multichannel acquisition were used to demonstrate the feasibility of the proposed method. Experimental results have shown that the newly introduced linear predictability prior improves the reconstruction quality of the T2-weighted images and benefits the subsequent T2 mapping by achieving high-speed, high-quality T2 mapping compared with the existing fast T2 mapping methods.

Conclusion: This work proposes a novel fast T2 mapping method integrating the linear predictable property of the exponential decay into the reconstruction process. The proposed technique can effectively improve the reconstruction quality of the state-of-the-art fast imaging method exploiting image sparsity and spatiotemporal low rankness. **Magn Reson Med 000:000–000, 2016.** © **2016 Wiley Periodicals, Inc.**

Key words: T2 mapping; exponential parameterization; linear predictability; Hankel low rank approximation; joint sparsity constraint; low-rank constraint; constrained reconstruction

INTRODUCTION

Quantitative evaluation of T2 relaxations have become increasingly important in a variety of research studies and clinic applications, such as iron overload (1), cartilage disease (2), multiple sclerosis (3), and carotid plaque characterization (4). However, commercial T2 relaxometry techniques acquire multiple images at various echo times (TEs) resulting a relative long scan time, which is a major bottleneck in clinic utility.

To solve this problem, reduced encoding techniques grounded on the theory of parallel imaging (5) and sparse sampling (6,7) have been extensively developed and shown promising potential in accelerating MR acquisition. Among them, parallel imaging techniques (8–10) are the earlier ones being successfully adopted in various parameter mapping experiments for efficient acquisition. Besides, considering the intrinsic low degree of freedom of the target image series, additional constraints have recently been used in an extensive body of work for improved reconstruction, such as the sparsity constraint of the T2-weighted images (11,12) imposing spatial smoothness, the temporal sparsity penalty of the T2-decay (13) penalizing the temporal nonsmoothness and the low-rank property of the image series (14–17) promoting spatiotemporal redundancy. These constraints are relatively general and also suitable for many imaging applications, such as dynamic imaging. With parametric model involved, Doneva et al (18,19) developed a model-based dictionary to enable efficient sparse representation in the parametric-encoding dimension. Sénégas et al (20) derived a GRAPPA-like kernel based on a mono exponential model to exploit the data correlation in k-t space. We conjecture that further taking advantage of the knowledge of the parametric model would improve the reconstruction of the state-of-the-art methods.

In this work, we proposed a novel method that explicitly exploits the linear predictability of the T2 decay, which can be modeled as a linear combination of L exponentials, as prior information on top of the standard sparsity and spatiotemporal low-rank constrained reconstruction. Specifically, a linear combination of L exponentials is linearly predictable to the L-th order, which can further translate in the low-rankness of a Hankel

[1]Paul C. Lauterbur Research Centre for Biomedical Imaging, Shenzhen Institutes of Advanced Technology, Shenzhen, Guangdong, China.

[2]Beijing Center for Mathematics and Information Interdisciplinary Sciences, Beijing, China.

[3]Department of Biomedical Engineering and Department of Electrical Engineering, University at Buffalo, The State University of New York, Buffalo, New York, USA.

[4]Hong Kong Sanatorium and Hospital, Hong Kong, China.

Grant sponsor: the National Natural Science Foundation of China; Grant numbers: 11301508, 81120108012, 81328013, 61471350; Grant sponsor: the Natural Science Foundation of Guangdong; Grant numbers: 2015A020214019, 2015A030310314, 2015A030313740; Grant sponsor: the Basic Research Program of Shenzhen; Grant numbers: JCYJ2015 0630114942318, JCYJ20140610152828678, JCYJ20140610151856736; Grant sponsor: US National Science Foundation; Grant number: CBET-1265612.

*Correspondence to: Dong Liang, Ph.D., Paul C. Lauterbur Research Centre for Biomedical Imaging, Institute of Biomedical and Health Engineering, Shenzhen Institutes of Advanced Technology, Chinese Academy of Sciences, Shenzhen, Guangdong, China, 518055. E-mail: dong.liang@siat.ac.cn

Received 28 July 2015; revised 19 November 2015; accepted 20 November 2015

DOI 10.1002/mrm.26083

Published online 00 Month 2016 in Wiley Online Library (wileyonlinelibrary.com).

matrix. Linear predictability has been investigated in the Cadzow enhancement algorithm (21) and demonstrated useful in MRSI data denoising (22). An iterative nonlinear filtering framework was adopted to impose these three priors to the target images by performing corresponding filtering iteratively. Both simulated and in vivo experimental data from multichannel acquisition were used to substantiate the feasibility of the proposed technique in improving the quality of fast T2 mapping with respect to the state-of-the-art methods.

THEORY

Review: Low-Rank and Joint Sparsity Priors

The spatiotemporal function of the T2-weithed images $I(\mathbf{r},t)$ is known to be partially separable as (7):

$$I=\sum_{j=1}^{J}\phi_j(\mathbf{r})\varphi_j(t) \quad [1]$$

where $\varphi_j(t)$ denotes the temporal subspaces and $\phi_j(\mathbf{r})$ is the corresponding spatial coefficients. The above equation assumes that the profiles of the T2 decay at all spatial locations are highly redundant for small J, because they are linear combinations of a few J temporal basis functions with spatial varying weights. Accordingly, the Casorati matrix:

$$I=\begin{bmatrix} I(\mathbf{r}_1,t_1) & I(\mathbf{r}_1,t_2) & \cdots & I(\mathbf{r}_1,t_M)\\ I(\mathbf{r}_2,t_1) & I(\mathbf{r}_2,t_2) & \cdots & I(\mathbf{r}_2,t_M)\\ \vdots & \vdots & \vdots & \vdots\\ I(\mathbf{r}_N,t_1) & I(\mathbf{r}_N,t_2) & \cdots & I(\mathbf{r}_N,t_M)\end{bmatrix} \quad [2]$$

will have a rank at most of J ($J \ll M$). On the other hand, the redundancy assumption also suggests that the image function at each TE (i.e., columns of I) will have similar anatomical structure, thus sharing analogous coefficient sparsity in terms of support and intensity distribution. This prior information, which has been exploited in distributed compressed sensing (23), is known as joint sparsity. Consequently, the image reconstruction could use both low-rank and joint-sparsity priors which is formulated as:

$$\hat{I}=\underset{I}{\operatorname{argmin}}\,||\Psi I||_{2,1}+\lambda||I||_{*}\ s.t.\ ||F_uI-d||_2^2\le\sigma^2 \quad [3]$$

where $I\in\mathbb{C}^{N\times M}$ is the matrix form of the desired T2-weighted image function with N the total number of image pixels and M the echo train length (ETL), $F_u \in \mathbb{C}^{U\times N}$ is the undersampled Fourier encoding matrix with $U \ll N$, $d\in\mathbb{C}^{U\times M}$ is the undersampled k-space data, and $\Psi\in\mathbb{C}^{N\times N}$ is the sparsifying operation matrix (Daubechies 4 wavelet in this work). To promote joint sparsity and low rankness, both the mixed L2–L1 norm of the sparse coefficients $||\alpha||_{2,1}=\sum_n\sqrt{\sum_m||\alpha_{nm}||^2}$ ($\alpha_{nm}=\psi_nI(t_m)$ and ψ_n denotes the n-th sparsifying basis function) and the nuclear norm of I (i.e., summation of singular values, which is the closest convex relaxation of the rank penalty) are usually minimized. Data consistency is exploited as an additional constraint, where σ^2 is proportional to the noise level controlling the tolerance in measurement consistency.

Linear Predictability of Linear Exponential Combinations

Consider a discrete time domain signal (i.e., $m=1,2,3,\ldots$) as a linear combination of L exponential functions with the general form of

$$s_0[m]=\sum_{l=1}^{L}\alpha_l e^{-\beta_l m\Delta t} \quad [4]$$

where Δt is the sampling interval, α_l denotes the combination weight and β_l is the decay rate. An important property of Eq. [4] is that the discrete signal $s_0[m]$ is linearly predictable to the L-th order (21):

$$s_0[m]=\sum_{l=1}^{L}\gamma_l s_0[m-l]. \quad [5]$$

Namely, the current intensity of $s_0[m]$ can be predicted as linear summation of its previous L values. γ_l represents the summation weight. Thereby, the Hankel matrix formed by $s_0[m]$

$$H[s_0]=\begin{bmatrix} s_0(1) & s_0(2) & \cdots & s_0(K)\\ s_0(2) & s_0(3) & \cdots & s_0(K+1)\\ \vdots & \vdots & \vdots & \vdots\\ s_0(M-K+1) & s_0(M-K+2) & \cdots & s_0(M)\end{bmatrix} \quad [6]$$

will have a low rank of L as long as $s_0[m]$ has the form of Eq. [4]. The proof of linear predictability and Hankel low-rankness can be found in the Appendix.

Proposed Formulation

The temporal signal $I(\mathbf{r},t_m)$ of a T2-weighted image series generated by a Carr-Purcell-Meiboom-Gill (CPMG) spin echo sequence can be written in a general form as:

$$I(\mathbf{r},t_m)=\sum_{l=1}^{L}\rho_l(\mathbf{r})\exp[i\theta(\mathbf{r})]\exp[-m\Delta t/\mathrm{T}_2(\mathbf{r})] \quad [7]$$

where $\rho_l(\mathbf{r})$ and T_2 represent the proton density distribution function and the T2 relaxation values of the l-th tissue compartment, respectively. θ denotes the image phase supposed to be shared at all TEs. $\mathbf{r}$ indicates spatial coordinate. $t_m=m\Delta t$ stands for the m-th TE with Δt the echo spacing. L is the number of linearly combined exponential terms (i.e., tissue compartments), which is application (or tissue) dependent. For instance, in the three-pool model of white matter, the white matter tissue is comprised of a myelin water pool, a myelinated axon water pool and a mixed water pool, yielding $L=3$. Actually Eq. [7] can be written in the form of Eq. [4] such that $I(\mathbf{r},t_m)$ is L-th order linear predictable:

$$I(\mathbf{r}, t_m) = \sum_{l=1}^{L} \gamma_l I(\mathbf{r}, t_{m-l}). \quad [8]$$

Thus, a Hankel matrix can be formed for $\forall \mathbf{r} \in \Omega$ (Ω denotes the region of interest)

$$H[I(\mathbf{r})] = \begin{bmatrix} I(\mathbf{r}, t_1) & I(\mathbf{r}, t_2) & \cdots & I(\mathbf{r}, t_K) \\ I(\mathbf{r}, t_2) & I(\mathbf{r}, t_3) & \cdots & I(\mathbf{r}, t_{K+1}) \\ \vdots & \vdots & \vdots & \vdots \\ I(\mathbf{r}, t_{M-K+1}) & I(\mathbf{r}, t_{M-K+2}) & \cdots & I(\mathbf{r}, t_M) \end{bmatrix} \quad [9]$$

which has a low rank of L. Generally, the Hankel matrix is designed as square as possible such that we chose K as the nearest integer greater than or equal to half of the ETL.

In practice, the T2 decay in some most commonly used T2 mapping sequences (e.g., turbo spin echo) is not exactly exponential due to the interference of stimulated and indirect echoes (24). Thus, the temporal evolution may deviate from the model in Eq. [7]. This issue is similar to the one in MR spectroscopy where the spectrum deviates from Lorentzian lineshape due to magnetic field inhomogeneity, limited spatial resolution, etc., but still can be fitted using a linear combination of more Lorentzian basis functions (25,26). Because the temporal evolution and the spectrum are related by Fourier transform, the temporal evolution could also be represented as a linear combination of more exponential decays. Therefore, Eq. [7] is still valid mathematically yet with the compromise that L is larger than the number of physically true water pools but usually smaller than half of the ETL in practice. Thus, the Hankel matrix could still be low-rank. A real in vivo brain dataset obtained with turbo spin echo will be used to demonstrate the low-rankness of the Hankel matrix in the experiment section.

With this knowledge, we can use such Hankel low-rankness as an essential prior of $I(\mathbf{r}, t)$ for sparse reconstruction (denoted as LP hereafter):

$$\hat{I} = \underset{I}{\operatorname{argmin}} ||F_u I - d||_2^2, \; s.t. \; rank\Big(H[I(\mathbf{r})]\Big) = L, \forall \mathbf{r}. \quad [10]$$

Equation [10] can be reformulated by means of minimizing the relaxed convex counterpart, namely the nuclear norm of the Hankel matrix over all spatial locations:

$$\hat{I} = \underset{I}{\operatorname{argmin}} \sum_{\mathbf{r}\in\Omega} ||H[I(\mathbf{r})]||_* \; s.t. \; ||F_u I - d||_2^2 \leq \sigma^2. \quad [11]$$

It is worth noting that the Casorati low-rankness considers the signal jointly by assuming that the temporal variations at various spatial locations are considerably similar (i.e., resulting in redundant information) while the Hankel low-rank approximation treats the signal variation at each spatial location independently, each following an exponential decay, which agrees with the T2 imaging model. Therefore, it is natural to integrate the Casorati low rankness with the Hankel low-rank approximation, while enforcing the joint sparsity prior. We propose to reconstruct the T2-weighted image functions with Model-driven low rank and sparsity priors (MORASA):

$$\begin{aligned} &\hat{I} = \underset{I}{\operatorname{argmin}} ||\Psi I||_{2,1} + \lambda ||I||_* + \gamma \sum_{\mathbf{r}\in\Omega} ||H[I(\mathbf{r})]||_* \\ &s.t. \sum_c ||F_u S_c \odot I - d_c||_2^2 \leq c\sigma^2 \end{aligned} \quad [12]$$

where $S_c \in \mathbb{C}^{N\times 1}$ indicates the sensitivity map of the c-th coil, d_c corresponds to the c-th coil data. Operator $\odot$ conducts point-wise multiplication of S_c with each column of I. The term model-driven low rank refers in particular to the Hankel low-rank approximation because it is driven by the linear predictability of the exponential parametric model.

To solve Eq. [12], we propose to use an efficient iterative nonlinear filtering (27) algorithm as described in Algorithm 1 assuming exact data consistency (i.e., $F_u S_c \odot I = d_c$). Because the cost function in Eq. [12] is convex (note that the operation of Hankel matrix formation $H[\cdot]$ is linear), the iterative algorithm could achieve convergence to the global minimum under the simple assumptions that all iterations of the algorithm lie within a bounded domain (28). Specifically, in each iteration, three nonlinear filtering operations are performed to enforce three corresponding priors, which is mathematically equivalent to minimizing a cost function promoting both the priors and the fidelity to the previous estimate. We use joint soft thresholding in the wavelet domain to enforce the joint sparsity. To promote low-rankness along the parametric direction in a simple way, we perform hard thresholding to empirically preserve the first 2$\sim$3 singular values or principal components (15) of the image Casorati matrix. Additionally, for the Hankel low-rank prior, we enforce the general low-rankness and Hankel structure alternately. First, we perform soft-thresholding on the singular values to promote low rankness, because the optimal rank of the Hankel matrix may vary from location to location and hard thresholding could be sensitive to spatial signal contamination due to undersampling. Second, the Hankel structure can be restored by taking the mean of all the antidiagonal elements and replacing each element by its mean value. We denote this operation as:

$$\hat{H} \equiv \text{Hankelize}(\hat{H}_0). \quad [13]$$

Afterward, the corresponding elements of $\hat{H}$ can be extracted to update the signal estimate $\hat{I}(\mathbf{r})$ for each spatial location. When enforcing data consistency, coil sensitivities from multichannel acquisitions are incorporated into the reconstruction (29). In addition, we enforce data consistency right after each nonlinear filtering to prevent any bias during a nonlinear filtering from propagating to the next one. At convergence, this iterative algorithm finds an approximated minimum of the constrained optimization problem in Eq. [12]. The entire diagram of the proposed MORASA method is illustrated in Figure 1.

METHODS

Both simulated and in vivo experimental datasets were used to validate the proposed method. In the in vivo

Algorithm 1. Iterative Nonlinear Filtering Approach for MORASA

MORASA

Input: Undersampled multichannel data d_c; Estimate the sensitivity maps S_c.

Initialization: Initial image estimate $I_0 = \sum_c (F_u^H d_c) \odot S_c^*$; iteration index $k = 0$.

Iteration: do {

1. sparsity prior
   a) $\alpha_k = \Psi I_k$, $\alpha_{k+1} = \text{JointSoftThresh}(\alpha_k, \tau)$, $I_{k+1} = \Psi^{-1}\alpha_{k+1}$, where
   $\text{JointSoftThresh}(\alpha_{nm}, \tau) = \alpha_{nm} / \sqrt{\sum_{m=1}^{M} ||\alpha_{nm}||_2^2} \cdot \max(0, \sqrt{\sum_{m=1}^{M} ||\alpha_{nm}||_2^2} - \tau)$, n and m are the indexes of sparsifying basis function and timeframe, respectively. Function $\max(\cdot)$ returns the larger value of the two inputs.
2. data consistency: $I_{k+1} = \sum_c \left[F_v^H F_v (I_{k+1} \odot S_c) + F_u^H d_c\right] \odot S_c^*$, F_v denotes the Fourier encoding operation at nonacquired k-space locations.
3. low rank prior
   a) $[U\,\Sigma\,V] = \text{SVD}(I_{k+1})$, $I_{k+1} = \sum_{j=1}^{J} U_j \Sigma_{j,j} V_j^H$
4. Data consistency as step 2.
5. Linear predictability prior, for $\forall \mathbf{r} \in \Omega$
   a) $[u\,\sigma\,v] = \text{SVD}\left(H[I_{k+1}(\mathbf{r})]\right)$, $\sigma = \max(\sigma - \upsilon, 0)$
   b) $\hat{H}(\mathbf{r}) = \text{Hankelize}(u\sigma v^H)$, extract $I_{k+1}(\mathbf{r})$ from $\hat{H}(\mathbf{r})$
6. Data consistency as step 2, $k = k + 1$.

} till convergence or maximum number of iterations.

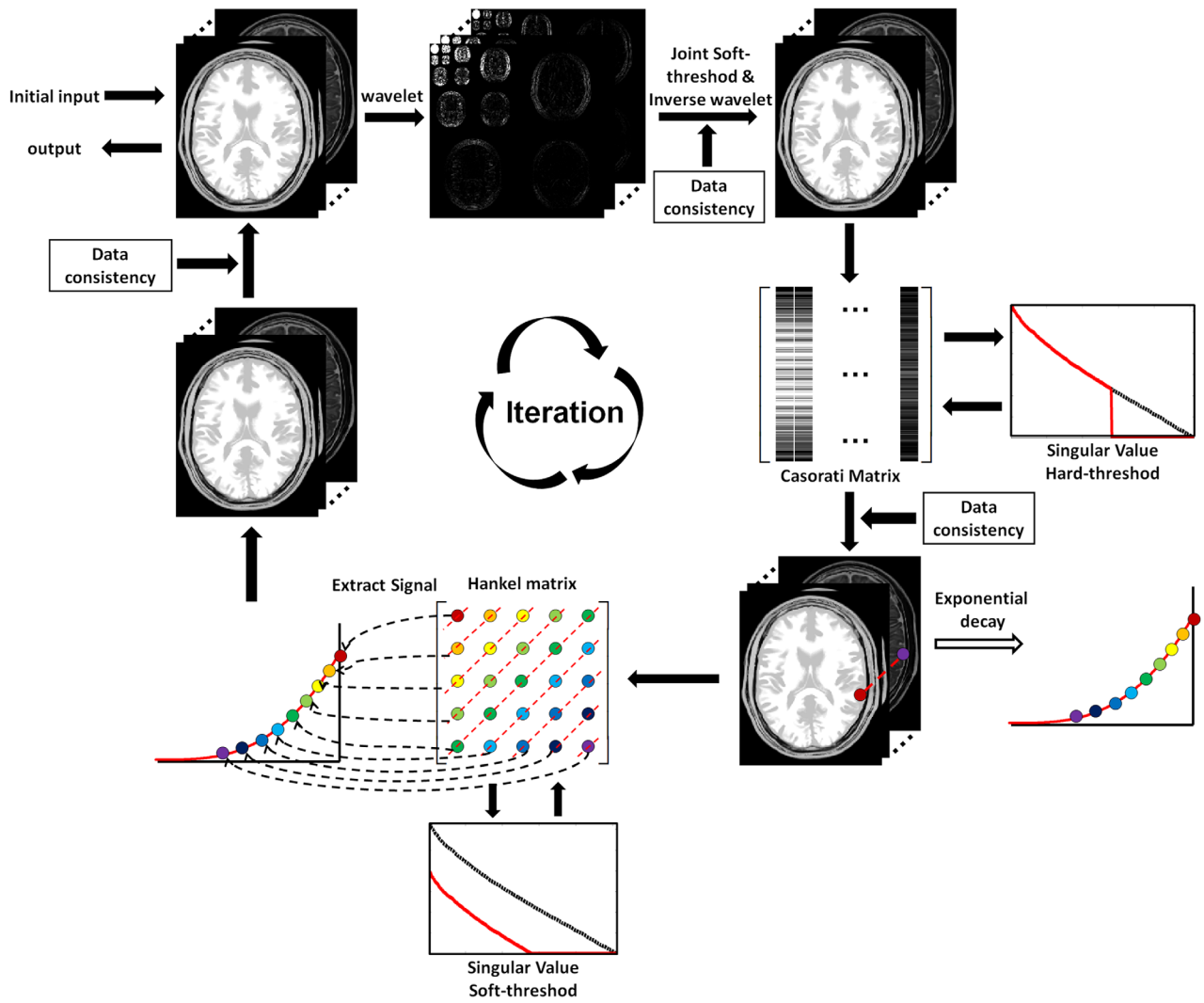

FIG. 1. The flow diagram of the proposed MORASA method for exponential parameterization of T2 relaxation.

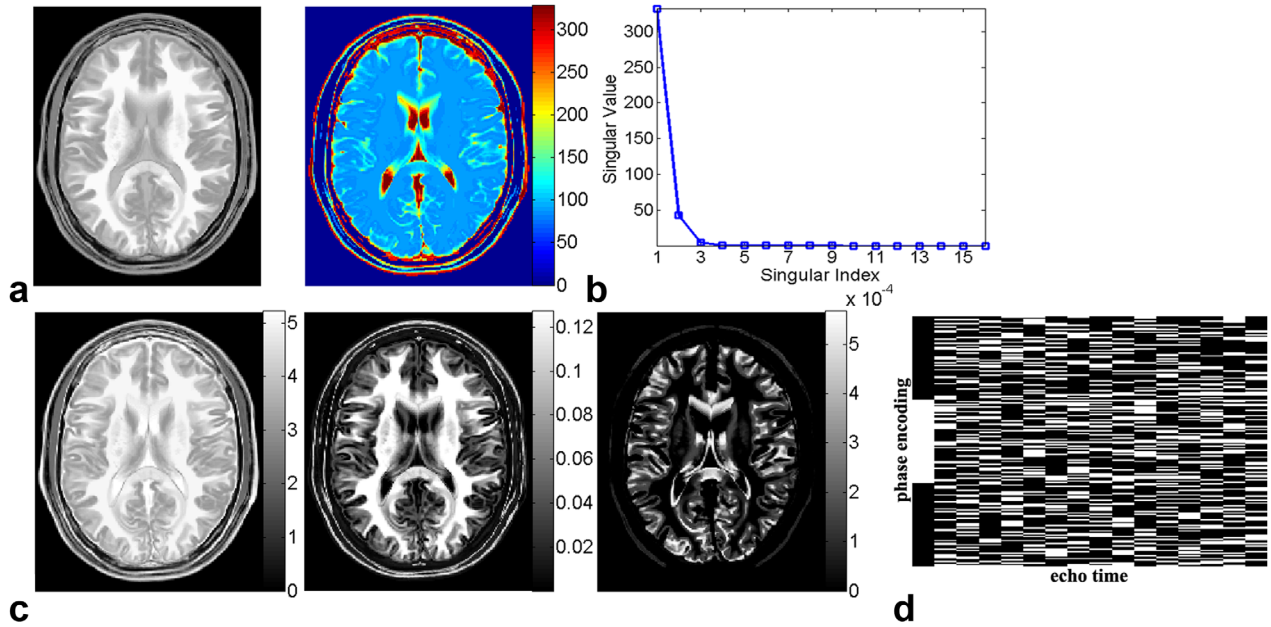

FIG. 2. The simulated brain phantom dataset. **a**: The ground truth T2 weighted image at the third TE (30 ms) and the T2 map. **b**: Singular values of the Casorati image matrix. **c**: The first, second and third singular values (from left to right) of the Hankel variant of the temporal decay at all spatial locations. **d**: The undersampling pattern adopted in this work for T2 mapping. The vertical direction indicates phase encodings and the horizontal direction denotes temporal dimension with 16 short intervals representing frequency encodings at various TEs.

experiments, informed consent was obtained from the imaging subject in compliance with the Institutional Review Board policy. The subject was immobilized by foam pads and requested to hold as still as possible to prevent motion artifacts. All the methods in comparisons were tuned to provide their best performance and all algorithms were implemented in Matlab (The Mathworks, Natick, MA). To estimate the T2 values, standard nonlinear least square fitting method was performed in the selected region-of-interest on a pixel-by-pixel basis. T2 relaxation values outside the reasonable range were excluded from the T2 map.

Simulation

For the simulation, we used a realistic digital brain phantom (30) which is synthesized as a linear combination of various tissue compartments. A series of spin echo T2-weighted images was generated (image matrix 220×180, ETL 16, first TE 10 ms and echo spacing 10ms) using the default brain tissue parameters. Specifically, for tissues such as cerebrospinal fluid (CSF) (similar for gray matter, fat, muscle skin, skin, skull and glial), we used the monoexponential model (i.e., $S_{\mathrm{CSF}} = \rho_{\mathrm{CSF}}[1 - \exp(-\mathrm{TR}/\mathrm{T1}_{\mathrm{CSF}})]\exp[-\mathrm{TE}/\mathrm{T2}_{\mathrm{CSF}}]$), where ρ_{CSF}, $\mathrm{T1}_{\mathrm{CSF}}$, $\mathrm{T2}_{\mathrm{CSF}}$ are default proton density, T1, and T2 values of CSF, respectively, provided in Pruessmann et al (29). For white matter, we used the biexponential model (i.e., $S_{\mathrm{WM}} = \rho_{\mathrm{WM}}[1 - \exp(-\mathrm{TR}/\mathrm{T1}_{\mathrm{WM}})][\exp(-\mathrm{TE}/\mathrm{T2}_{\mathrm{WM1}}) + \exp(-\mathrm{TE}/\mathrm{T2}_{\mathrm{WM2}})]$) with $\mathrm{T2}_{\mathrm{WM1}} = 40\mathrm{ms}$ and $\mathrm{T2}_{\mathrm{WM2}} = 130\mathrm{ms}$. Finally, the brain phantom was obtained as the summation of all the tissue compartments. The T2-weighted image at the third TE (30 ms) along with the T2 relaxation maps calculated by means of the monoexponential least-square fitting are displayed in Figure 2a. The singular values of the Casorati image matrix are plotted in Figure 2b, confirming the low rankness.

Figure 2c shows (from left to right) the map of the first, second, and third singular values of the Hankel matrixes at all spatial locations. As can be seen, the temporal variation at most spatial locations contains at least one dominant T2 component (i.e., corresponds to the first singular value) and at some locations (i.e., mostly while matter in this case) consists of another insignificant T2 component (i.e., corresponds to the second singular value). The appearance of the second T2 component can also be resulted from the superposition of different tissue compartments. Figure 2c demonstrates that the temporal evolution indeed possesses a low-rank property in its Hankel variant. For the multi-channel acquisition case, each T2-weighted image was modulated by the sensitivity maps of an eight-channel head coil (complex valued) that were simulated based on the Biot-Savart's law (31). Spatial Fourier transform was applied to the simulated brain phantom to generate the full k-space data.

Retrospective undersampling was then performed to obtain the undersampled data. The undersampling pattern adopted in this work is shown in Figure 2d, which fully samples the central k-space region at the first TE and randomly samples the entire k-space with DC included at the other TEs (17). The same number of lines were acquired for each TE. This sampling pattern acquires a larger central region in the first echo to increase signal-to-noise ratio (SNR) of the reconstructed T2-weighted image series (17). And the uniform random undersampling at the other TEs caters to the incoherency

required in sparse reconstruction. Besides, in the context of parallel imaging, the broad fully sampled central region at the first TE can provide a better estimate of the coil sensitivity. With this dataset, we aim to comprehensively demonstrate the advantage of using the linear predictability prior in T2 mapping and the superiority of the proposed technique to the state-of-the-art methods at various reduction factors and noise levels.

Effectiveness of Linear Predictability Prior

We demonstrated the advantage of linear predictability prior over other constraints using a simulated single-channel brain phantom dataset at a reduction factor of 3. To enforce linear predictability, we tested three constrained reconstructions denoted as LP1, LP1&2, and LP*, respectively. For LP1, we solved the optimization problem in Eq. [10] with L=1 for all spatial locations, namely only Hankel matrix with explicit rank 1 constraint. For LP1&2, we still solved Eq. [10] but with L=2 for white matter (i.e., as shown in the second map of Figure 2c, the T2 decay in white matter is exactly 2^{nd}-order linear predictable) and $L = 1$ for other regions. For LP*, we solved the optimization problem in Eq. [11], minimizing the nuclear norm of the Hankel matrix with soft thresholding of the singular values for all spatial locations (i.e., iteratively conducted step 5 to step 6 in **Algorithm 1**).

Reconstructions with standard low-rank (LR) constraint and sparsity and low-rank (SLR) constraint were also implemented for comparison. Specifically, for LR constrained reconstruction, we used hard thresholding of the singular values of the Casorati matrix (i.e., iteratively conducted step 3 and step 4 in **Algorithm 1**). For SLR constrained reconstruction, we further integrated joint soft thresholding of the wavelet coefficients of the T2-weighted images (i.e., iteratively conducted step 1 to step 4 in **Algorithm 1**).

Finally, we integrated LP* with SLR (denoted as SLR-LP) to substantiate the ability of LP in improving the state-of-the-art method. To clarify, SLR-LP is the single coil version of the proposed method. LP*, LR, and SLR are also reconstructions for single coil data here. Thus, to implement these methods, the data consistency step in **Algorithm 1** should be adjusted to the single coil version accordingly. To achieve the best performance, overestimated rank constraint (i.e., $J = 2$) was adopted for the conventional LR and SLR method. While for the proposed SLR-LP method, we chose $J = 3$. The threshold of the wavelet coefficients τ and the threshold of the singular values of the Hankel matrixes ν were set to be 0.01 and 0.1, respectively.

Method Comparison with Multichannel Acquisitions

We compared the reconstructed images and T2 maps of different methods using the simulated multichannel brain phantom data at various reduction factors (R = 3, 4, 6, 8) for both noiseless and noisy circumstances. Complex Gaussian noise was added to the brain phantom to simulate a low SNR situation (SNR = 20) where SNR is defined as the ratio of the mean signal intensity of the T2-wighted image series to the noise standard deviation. A low-rank based method k-t PCA/SENSE (14) and a state-of-the-art sparsity and low-rank based method (denoted as SLR/SENSE hereafter) were both used for comparison. For k-t PCA/SENSE, regular downsampling in k-t space was adopted as described in the original paper (14). For SLR/SENSE and MORASA, the undersampling shown in Figure 2d was adopted. All methods used the same sensitivity maps. To accurately estimate the principal components in the k-t PCA/SENSE method, the central region of k-space (i.e., the same amount of lines as is used to estimate the sensitivity map) was assumed available at all the TEs so as to ensure its best performance. Additionally, the SLR/SENSE method was implemented in the same framework as depicted in **Algorithm 1** except that the linear predictability constraint was not performed. The optimal parameters are consistent for all the reduction factors. Specifically, we set $J = 3$, $\upsilon = 0.1$, $\tau = 0.01$ and $\tau = 0.02$ for the noiseless and low SNR case, respectively.

In Vivo Experiment

Human Brain T2 Mapping

To validate the proposed method in vivo, a fully sampled multicontrast brain dataset was acquired on a 3 Tesla (T) scanner (MAGNETOM Trio, SIEMENS, Germany) using a turbo spin echo sequence with a 12-channel head coil array [matrix size = 192×192, field of view (FOV) = 192 mm × 192 mm, slice thickness = 3.0 mm, ETL = 15, ΔTE = 8.8 ms, repetition time (TR) = 4000 ms, bandwidth = 362 Hz/pixel]. The total scan time is 12 min and 54 s. The undersampled data were retrospectively obtained using the sampling pattern shown in Figure 2d at reduction factors of 4, 6, and 8. The SLR/SENSE method was conducted for comparison. Other experiments settings were similar to those in the brain phantom case. We set $J = 3$, $\tau = 0.005$, and $\upsilon = 0.02$ for the proposed method with all the reduction factors. As mentioned before, we use this in vivo dataset to validate the Hankel low-rankness in the case where the T2 decay may be affected by the stimulated and indirect echoes. Typically, we adaptively combined the fully sampled multichannel data into a single-channel complex dataset using the adaptive combine method (32). Then we computed the singular values of the Hankel matrixes at all spatial locations and showed the first three singular value maps in Figure 7a. As can be seen, the first singular values (i.e., corresponding to a single exponential component) dominate at most spatial locations indicating that the Hankel matrix formed from the T2 decay of real T2-weighted image series is approximately low-rank at most spatial locations.

Human Knee T2 Mapping

To validate the proposed technique, a human knee experiment was also conducted on a 3T scanner (MAGNETOM Trio, Siemens) using a multicontrast turbo spin echo sequence with an eight-channel flexible coil array (matrix size = 128×128, FOV = 128mm × 128 mm, slice thickness = 3.0 mm, ETL = 10, TE = 17 ms∼93.5 ms with ΔTE 8.5 ms, TR = 1500 ms, bandwidth = 355 Hz/pixel).

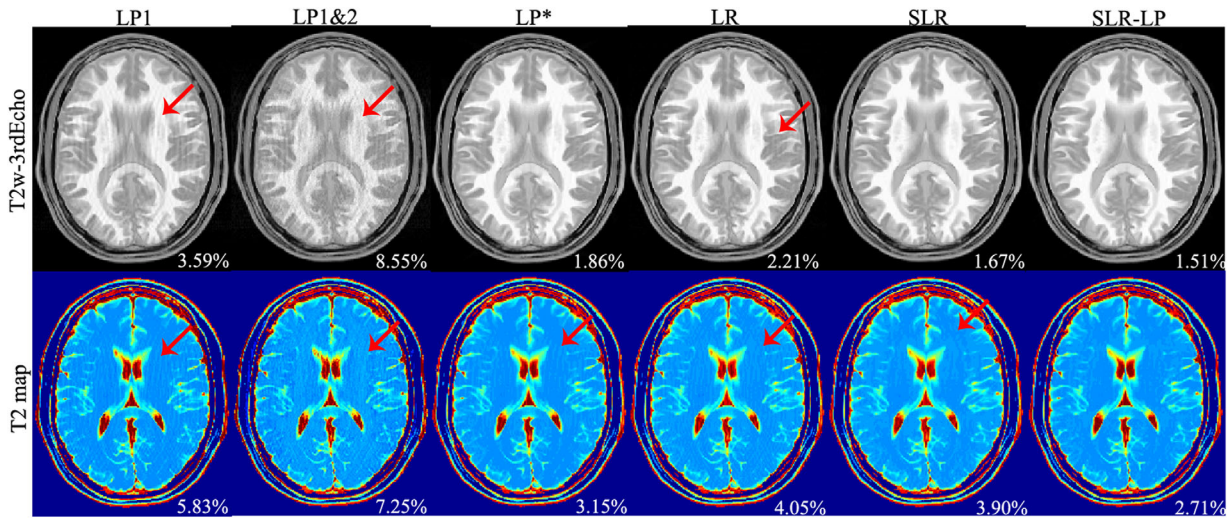

FIG. 3. The reconstruction results of various constrained methods based on the single channel version of the brain phantom data at a reduction factor of 3. The percentage numbers denotes the nRMSEs of corresponding T2-weighted image series and T2 maps.

The total scan time is 6 min and 29 s with over-samplings along the phase encoding direction. Undersampled k-space data was retrospectively obtained using the sampling pattern shown in Figure 2d at reduction factors of 4, 6, and 8. The coil sensitivity maps were estimated from the acquired k-space data at the first TE (17 ms) and assumed to be the same for all the TEs which were then used for both SLR/SENSE and the proposed MORASA methods. We set $J = 2$, $\tau = 0.02$, and $\upsilon = 0.06$ for the proposed method with all the reduction factors. Three cartilage regions of interest were selected (Figure 8. Bottom left) to quantitatively access the performance of the reconstruction methods by comparing the mean value and the standard deviation.

Evaluation

Both the quality of the reconstructed image series and the subsequent estimated T2 map can be quantified with the normalized root-mean-square error (nRMSE):

$$e = \sqrt{\frac{||\hat{s} - s_0||_2^2}{||s_0||_2^2}} \times 100\% \qquad [11]$$

where $\hat{s}$ and s_0 denote the reconstructions from undersampled and fully sampled data, respectively. Moreover, the T2 maps were masked before computing the nRMSE to restrict our evaluation to the tissue of interest and exclude unmeaningful values.

RESULTS

Simulation

Effectiveness of Linear Predictability Constraint

Reconstructions of the single-channel brain phantom using different constraints are shown in Figure 3. We first compared different implementations of the LP prior, named LP1, LP1&2, and LP*. As can be seen, although the LP1&2 constraint exploits the biexponential model in the white matter, the LP1-constrained method still performs much better than the LP1&2-constrained method in terms of both reconstruction error and T2 relaxation error. This is probably because the smaller singular value of the Hankel matrix (reflecting a short T2 component) is prone to severe contamination by the larger singular value of the Hankel matrix (mainly reflecting a long T2 component) at an adjacent voxel due to undersampling. Even if a high-quality initial value (e.g., the reconstruction of the SLR method) is used (results not shown here), LP1 is still superior to LP1&2. Moreover, compared with LP*, both LP1 and LP1&2 reconstructions present obvious aliasing artifacts in the T2-weighted image and T2 map, which suggests that directly restricting the order (i.e., hard-thresholding) of linear predictability of the T2 decay is quite sensitive to spatial signal contamination in sparse reconstruction. Therefore, we propose to minimize the nuclear norm of the Hankel matrix (i.e., using soft-thresholding), which is shown to effectively alleviate the aliasing artifacts in both the T2-weighted images and the T2 map.

Compared with the LP* constraint, the LR constraint leads to severer aliasing artifacts in the T2-weighted image and the T2 relaxation map. With the additional joint sparsity constraint (i.e., SLR reconstruction), the aliasing artifacts are alleviated but still noticeable. Finally, with additional LP constraint, the aliasing artifacts are visually suppressed and the reconstruction errors are significantly reduced, suggesting that the linear predictability prior is actually complementary to the sparse and low-rank priors and is capable of improving the state-of-the-art methods in T2 mapping.

Method Comparison with Multichannel Acquisitions

The estimated T2 maps using k-t PCA/SENSE, SLR/SENSE and the proposed MORASA methods at various reduction factors are shown in Figure 4 (noiseless case) and Figure 5 (low SNR case). We can see that k-t PCA/SENSE produces noticeable aliasing artifacts in the T2 map (red arrow) even at a low reduction factor of R = 3. As the reduction factor increases, the estimation error increases. The SLR/SENSE method is able to suppress the aliasing artifacts and preserve more image details at

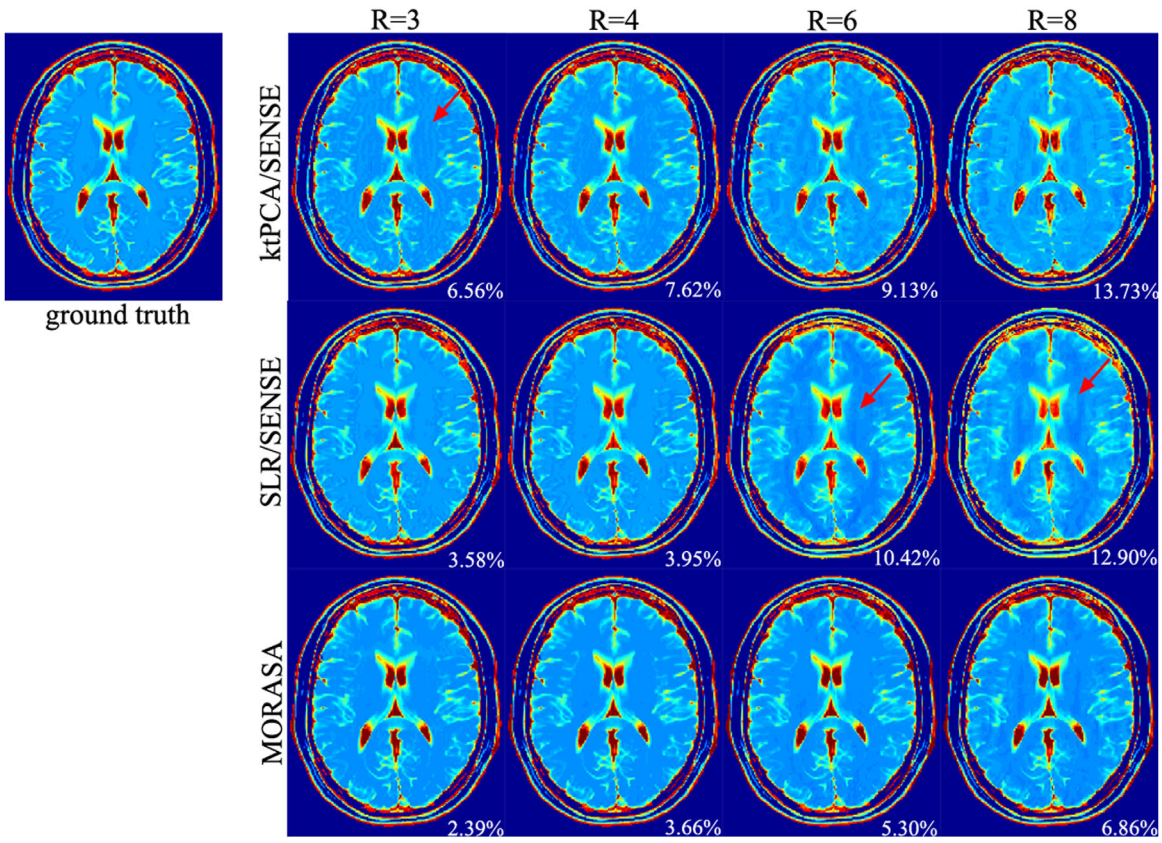

FIG. 4. Estimated T2 maps from the reconstructions of k-t PCA/SENSE, SLR/SENSE and MORASA methods using the multichannel brain phantom dataset (noiseless) at reduction factors of R = 3, 4, 6, and 8. The percentage numbers are the nRMSEs of the corresponding T2 maps.

low reduction factors, but the T2 estimation error starts to increase at R = 6 and R = 8 (shown as inhomogeneous region indicated by red arrows). The proposed MORASA method outperforms the other two methods in terms of suppressed artifacts and improved T2 accuracy at all reduction factors. In particular, the aliasing artifact in the T2 map is considerably suppressed even at R = 8. In the noisy circumstance, the proposed MORASA method also exhibits superior performance to the other two methods at all reduction factors. Figure 6 plots the T2-weighted image reconstruction error of the SLR/SENSE and MORASA methods as a function of iteration numbers at R = 6 in the noiseless case where the convergence of the proposed method can be observed. Moreover, the proposed MORASA method also converges faster (i.e., at the 15^{th} iteration approximately) than the SLR/SENSE method (i.e., at the 80^{th} iteration approximately). However, the computational cost per iteration is increased due to the LP constraint. The computer running time of the k-t PCA/SENSE, SLR/SENSE and the proposed MORASA method are 120 (50 CG iterations), 323 (80 iterations), and 302 (15 iterations) seconds, respectively.

In Vivo Experiment

Human Brain T2 Mapping

The estimated T2 maps of the human brain data (two slices) using the state-of-the-art SLR/SENSE and the proposed MORASA method are shown in Figures 7b,c. In general, the proposed MORASA method outperforms the SLR/SENSE method in terms of T2 accuracy and suppressed aliasing artifacts at all reduction factors. Specifically, the SLR/SENSE method provides good results at R = 4 and R = 6 visually. Detail loss and aliasing artifacts become severe and unacceptable as the reduction factor increases to 8. In contrast, the proposed MORASA method maintains more details and exhibits less aliasing artifacts in the T2 map than the SLR/SENSE method, thus generating consistently smaller T2 nRMSE at all reduction factors. Even at R = 8, the proposed method produces rather accurate T2 estimations. The means and standard deviations of the T2 values in selected regions of interest (ROIs) (indicated by the red rectangular box in Figures 7b,c) are presented in Table 1.

Human Knee T2 Mapping

The reconstructed T2 maps of the human knee are shown in Figure 8. nRMSE in regions with T2 value ranging from 30 to 45 ms have also been calculated. Besides, we selected three cartilage ROIs and compared the mean and standard deviation (SD) of the T2 values in Table 2. We can see that the proposed MORASA method consistently surpasses the state-of-the-art SLR/SENSE method at all reduction factors in terms of smaller nRMSEs and more accurate mean and standard deviation within all ROIs. Similar conclusion can be

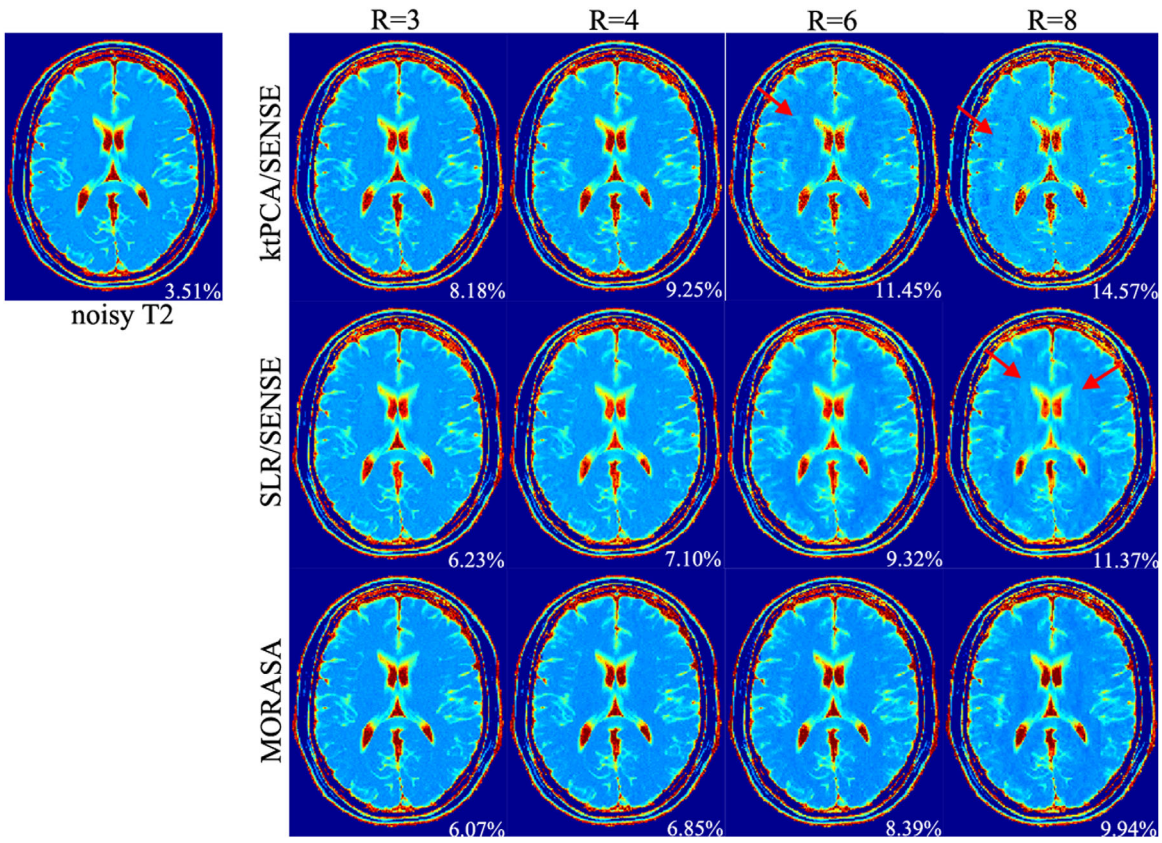

FIG. 5. Estimated T2 maps from the reconstructions of k-t PCA/SENSE, SLR/SENSE and MORASA methods using the multichannel brain phantom dataset (low SNR) at reduction factors of R = 3, 4, 6, and 8. The percentage numbers are the nRMSEs of the corresponding T2 maps.

made as in the previous simulation and human brain T2 mapping case that the proposed MORASA method can provide more accurate T2 estimation than the state-of-the-art SLR/SENSE method.

DISCUSSION

Relationship with Existing Method

This work proposed a novel image reconstruction method for parameterization of T2 relaxation. Distinguished from previous sparse reconstruction methods which only take advantage of general priors of the image series such as joint sparsity and spatiotemporal low-rankness, we proposed to incorporate priors directly from the parametric model into the reconstruction, namely the linear predictability of the exponential decay, to enable improved image reconstruction and more accurate parameter fitting. The LP constraint offers prior information complementary to the existing sparse and low-rank constraint, exhibiting superior performance to

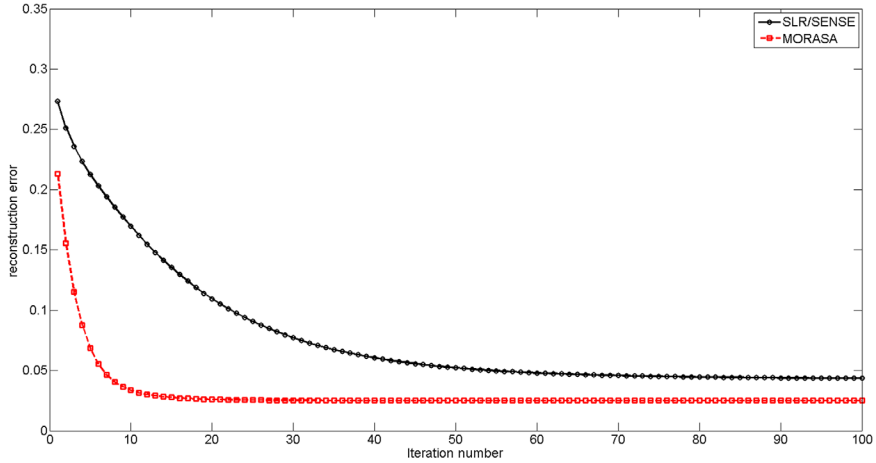

FIG. 6. The nRMSE of the T2-weighted image series of the SLR/SENSE and MORASA methods using the multichannel brain phantom dataset as a function of iteration numbers at a reduction factor of 6.

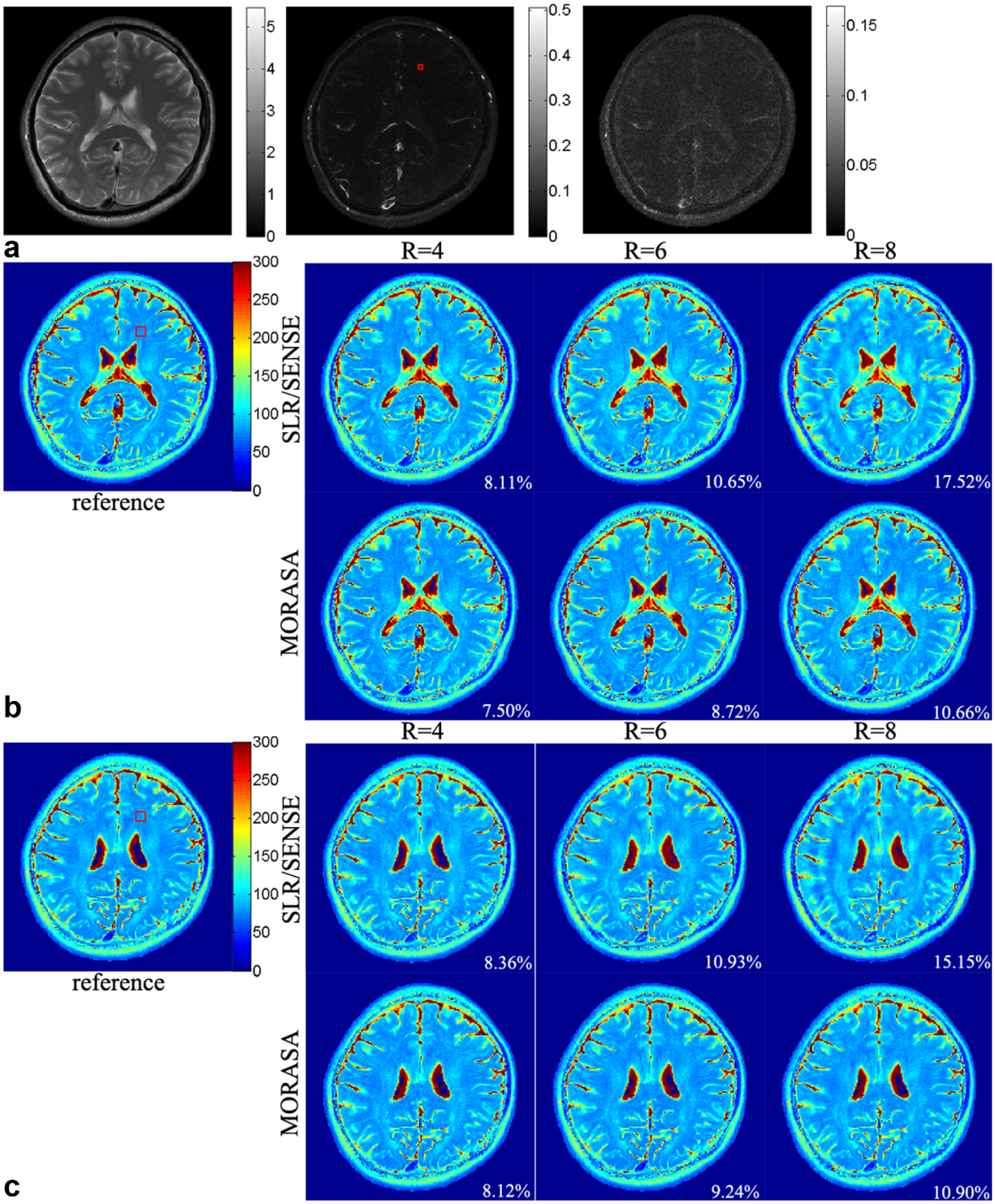

FIG. 7. **a**: The first three singular value maps (from left to right) of the Hankel matrix formed from the T2 decay of the human brain dataset. **b,c**: The estimated T2 maps of the human brain (slice 8 and slice 3) from the reconstruction of SLR/SENSE and MORASA methods at reduction factors R = 4, 6, 8. The percentage numbers are the nRMSEs of the corresponding T2 maps. The reference T2 map is estimated from the fully sampled k-space data.

the state-of-the-art methods. However, the proposed method needs to tune an additional parameter to enforce the Hankel low-rankness, which may vary from different applications.

The newly introduced LP constraint also causes an increase of reconstruction time compared with conventional method. Enforcing the LP constraint for a single pixel is fast (i.e., operating on small sized matrix), while

Table 1
Means and SDs of the T2 Values in Selected ROIs of the Human Brain Dataset

	R=4	R=6	R=8	R=4	R=6	R=8
Gold standard Mean (std)	3rd Slice 81.46 (4.53)			8th Slice 78.77 (2.62)		
SLR/SENSE	81.87 (4.55)	84.02 (4.72)	83.38 (4.08)	80.21 (3.16)	81.28 (3.01)	82.87 (4.10)
MORASA	**81.24** (4.42)	**81.79** (4.16)	**81.66** (3.97)	**78.60** (3.29)	**78.62** (3.15)	**79.17** (3.14)

enforcing it over all spatial locations could be time-consuming. Theoretically, parallel computing can be adopted to accelerate this process. Besides, due to the effectiveness of the LP constraint, the proposed method would converge with much less iterations (i.e., five times fewer iterations for the brain phantom) than the conventional method. Thus, by means of using parallel computing and early termination, the increase of reconstruction time of the proposed method should be tolerable practically.

As another fast parameter mapping approach using the parametric model, model-based reconstruction (33–39) methods directly estimate the parameter maps from undersampled k-space data and, therefore, have much reduced degree of freedom. The major difference between model-based reconstruction and the proposed method is that the former directly regularizes the sparsity of the relaxation map (34), while the latter takes advantage of the exponential parametric model in a relaxed sense to balance the trade-off between the data consistence and the exponential structure. Thus, the proposed method is suitable for cases where the T2-weighted image series is also of significant diagnosis interest. Besides, the model-based methods will be computational expensive when being extended to a multiexponential model.

Parameter Selection

To solve Eq. [12], we proposed an iterative nonlinear filtering approach as describe in **Algorithm 1**. Specifically, three parameters in this approach need to be carefully selected: the rank of the Casorati matrix J, the threshold of the wavelet coefficients τ and the threshold of the singular values of the Hankel matrixes ν. As shown in previous work (14,15,17), explicit rank constraint is effective enough to be adopted to enforce low-rankness along the parametric direction. Besides, rank selection is relatively simple compared with tuning the soft threshold in various cases. In general, the selection of J could differ from applications. We found empirically that setting $J = 3$ enables the best reconstruction quality for the in vivo brain dataset, while the optimal choice for the in vivo knee dataset is $J = 2$. Besides, the optimal J may also vary with the reduction factor for different methods. For the in vivo brain dataset, $J = 2$ is necessary for the SLR/SENSE method to provide the best performance at high reduction factors (6 and 8), while $J = 3$ is optimal for the proposed MORASA method at all reduction factors, manifesting the capability of the LP constraint.

In addition to J, we need to select τ, which controls the strength of sparsity enforced in the reconstruction. τ can be decided by means of visual inspection from the results of using various threshold values. We observed that both SLR/SENSE and MORASA methods are quite stable with a relatively large range of threshold values. In practice, one useful way to select τ is to set it on the same order of magnitude as the noise power which can be estimated from the background of the image. Besides, we found empirically that the SLR/SENSE and MORASA methods in most cases share a similar value of τ.

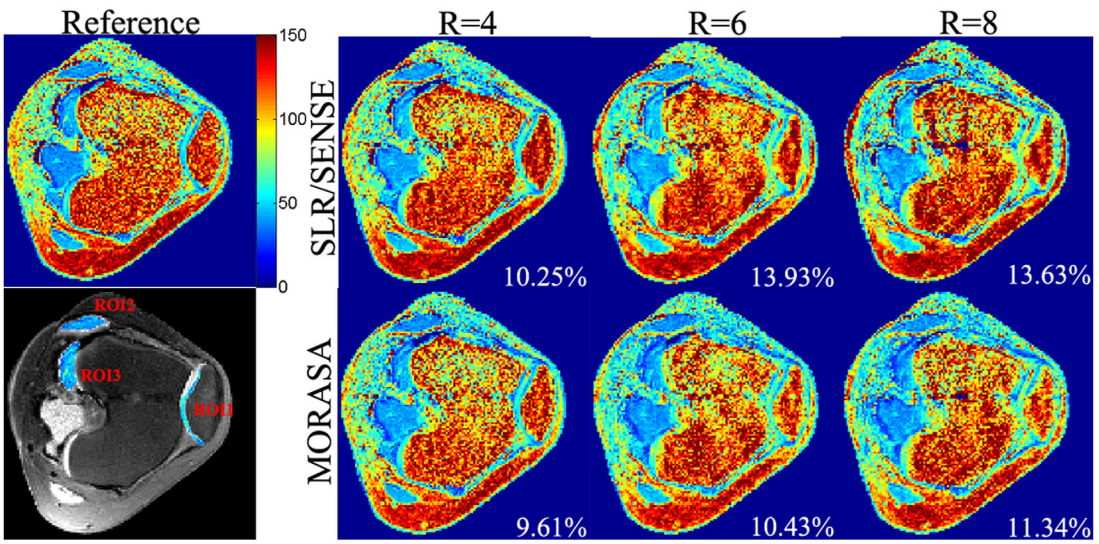

FIG. 8. The estimated T2 maps of the human knee using SLR/SENSE and MORASA reconstruction method at reduction factors of 4, 6, 8. Three ROIs were selected to quantitatively access the performance of the reconstruction methods. The percentage numbers are the nRMSEs in the regions with T2 value ranging from 30–45 ms.

Table 2
Means and SDs of the T2 Values in Selected ROIs of the Human Knee Dataset

	R=4	R=6	R=8	R=4	R=6	R=8	R=4	R=6	R=8
Gold Mean (std)	ROI 1 41.45 (7.63)			ROI 2 33.75 (4.41)			ROI 3 36.61 (7.91)		
SLR/SENSE	45.35 (9.26)	51.89 (13.49)	56.18 (15.80)	34.76 (4.27)	35.92 (4.17)	37.60 (5.53)	38.34 (7.39)	40.90 (8.07)	40.36 (8.09)
MORASA	**43.38** (8.28)	**48.34** (11.67)	**52.57** (13.68)	**32.81** (4.34)	**33.31** (3.88)	**34.64** (4.70)	**36.98** (7.41)	**36.79** (6.21)	**35.51** (6.57)

Last but not the least, we have to chose a proper ν to enforce the Hankel low-rankness. Theoretically, a proper ν is determined by the underlying T2 relaxation values, which would vary from applications. Empirically, we set ν on the same order of magnitude as the signal power in the "noise-like" region (e.g., the region indicated by the red box in Figure 7a) of the second singular map of the Hankel matrixes.

Requirement of the Hankel Low-Rankness

The low-rank property of the Hankel matrix declared in Eq. [6] does not require a shared proton distribution by all exponential decays, but does require equal TE spacing. With unequal TE spacing, the rank of the Hankel matrix will increase accordingly. Fortunately, we can always design protocols with equal TE spacing in most cases.

Iteratively Conducting Image Reconstruction and Parameter Mapping

The idea of the proposed technique is similar to conducting image reconstruction and parameter mapping iteratively (40,41). Actually, in the original Cadzow enhancement algorithm (21), Hankel low-rank approximation is achieved by performing Eq. [8] and Eq. [9] alternately for infinite times (or till convergence). If we strictly enforce Hankel low rankness, the resulting signal extracted from the Hankel matrix will strictly obey exponential decay, which is equivalent to performing T2 mapping. However, the proposed method only performs Eq. [8] and Eq. [9] once per iteration (denote as inexact Hankel low-rank approximation), which still generates good results. This is probably because at the very beginning of the algorithm, the reconstruction may contain a lot of aliasing artifacts such that a strict Hankel low-rank approximation may cause severe fitting error besides the increased computing burden, while the inexact Hankel low-rank approximation is able to gradually impose linear predictability with iterations.

Limitation and Future Work

One limitation of the proposed method is that a uniform threshold is used to enforce the Hankel low-rankness over all spatial locations. However, it would be desirable to adopt spatially adaptive thresholds because the T2 relaxation values may vary significantly with spatial locations. Future work will also investigate applications in multiexponential parameterization and other exponential decay models such as T1rho mapping (42).

CONCLUSIONS

This work proposed to incorporate the exponential priors into the reconstruction of the T2-weighted image series from undersampled k-space data. The reconstruction problem was solved using an alternating nonlinear filtering method. Both simulation and in vivo results demonstrated the superiority of the proposed method to the state-of-the-art image reconstruction methods at different reduction factors and noise levels.

ACKNOWLEDGMENTS

Xi Peng thanks Prof. Zhi-Pei Liang with University of Illinois at Urbana-Champaign for the enlightening discussion at the early stage of this work. Xi Peng thanks Prof. Jianfeng Cai with Hong Kong University of Science and Technology for his kind help with the proof in the Appendix. This work was partly supported by the National Natural Science Foundation of China, the Natural Science Foundation of Guangdong, the Basic Research Program of Shenzhen, and US National Science Foundation.

APPENDIX

Proof of Linear Predictability

We say a discrete signals$s_0[m]$ is linear predictable to the L-th order if and only if it satisfies:

$$s_0[m] = \sum_{l=1}^{L} \gamma_l s_0[m-l] \qquad [A1]$$

Let us assume $s_0[m] = \sum_{l=1}^{L} \alpha_l e^{-\beta_l m \Delta t}$ and substitute it in Eq. [A1]:

$$\begin{aligned}
&\sum_{l=1}^{L} \alpha_l z_l^m = \gamma_1 s_0[m-1] + \gamma_2 s_0[m-2] + \cdots + \gamma_L s_0[m-L] \\
&= \gamma_1 \sum_{l=1}^{L} \alpha_l e^{-\beta_l (m-1)\Delta t} + \gamma_2 \sum_{l=1}^{L} \alpha_l e^{-\beta_l (m-2)\Delta t} + \cdots \gamma_L \sum_{l=1}^{L} \alpha_l e^{-\beta_l (m-L)\Delta t} \\
&= \sum_{l=1}^{L} \alpha_l \gamma_1 z_l^{m-1} + \alpha_l \gamma_2 z_l^{m-2} + \cdots \alpha_l \gamma_L z_l^{m-L}
\end{aligned} \qquad [A2]$$

where $z_l = e^{-\beta_l \Delta t}$. For the summation in Eq. [A2] holds, we could expect the equality holds for each l, yielding:

$$\alpha_l z_l^m = \alpha_l \gamma_1 z_l^{m-1} + \alpha_l \gamma_2 z_l^{m-2} + \cdots + \alpha_l \gamma_L z_l^{m-L} \qquad [A3]$$

Dividing $\alpha_l z_l^{m-L}$ on both side of Eq. [A3], we get:

$$z_l^L = \gamma_1 z_l^{L-1} + \gamma_2 z_l^{L-2} + \cdots + \gamma_L \qquad [A4]$$

To this end, if we could find coefficients $\gamma_1, \gamma_2, \cdots, \gamma_L$ satisfy Eq. [A4] for each l, the proof is done.

Actually, Eq. [A4] suggest that $z_1, z_2, \cdots, z_L$ are exactly the L solutions of the polynomial function $z^L = \gamma_1 z^{L-1} + \gamma_2 z^{L-2} + \cdots + \gamma_L$. Thus, we can rewrite Eq. [A4] as $(z - z_1)(z - z_2) \cdots (z - z_L) = 0$ and consequently find the linear predictable weights.

Proof of Hankel Low-Rankness

The Hankel matrix can be decomposed using matrix factorization as:

$$H = \begin{bmatrix} s_0[1] & s_0[2] & \cdots & s_0[K] \\ s_0[2] & s_0[3] & \cdots & s_0[K+1] \\ \vdots & \vdots & \vdots & \vdots \\ s_0[M-K+1] & s_0[M-K+2] & \cdots & s_0[M] \end{bmatrix} = Q \Sigma P$$

where $Q = \begin{bmatrix} 1 & 1 & \cdots & 1 \\ z_1 & z_2 & \cdots & z_L \\ z_1^2 & z_2^2 & \cdots & z_L^2 \\ \vdots & \vdots & \vdots & \vdots \\ z_1^{M-K} & z_2^{M-K} & \cdots & z_L^{M-K} \end{bmatrix}$, $\Sigma = \begin{bmatrix} \alpha_1 & & & \\ & \alpha_2 & & \\ & & \ddots & \\ & & & \alpha_L \end{bmatrix}$,

$P = \begin{bmatrix} z_1 & z_1^2 & \cdots & z_1^K \\ z_2 & z_2^2 & \cdots & z_2^K \\ \vdots & \vdots & \vdots & \vdots \\ z_L & z_L^2 & \cdots & z_L^K \end{bmatrix}$, $s_0[m] = \sum_{l=1}^{L} \alpha_l z_l^m$

As long as $\alpha_i \neq \alpha_j, \forall i \neq j$, $\mathrm{rank}(H) = \mathrm{rank}(\Sigma) = L$

REFERENCE

1. Pierre TG, Clark PR, Chua-anusorn W, Fleming AJ, Jeffrey GP, Olynyk JK, Pootrakul P, Robins E, Lindeman R. Noninvasive measurement and imaging of liver iron concentrations using proton magnetic resonance. Blood 2005;105:855–861.
2. Eckstein F, Burstein D, Link TM. Quantitative MRI of cartilage and bone: degenerative changes in osteoarthritis. NMR Biomed 2006;19: 822–854.
3. MacKay A, Whittall K, Adler J, Li D, Paty D, Graeb D. In vivo visualization of myelin water in brain by magnetic resonance. Magn Reson Med 1994;31:673–677.
4. Demarco JK, Rutt BK, Clarke SE. Carotid plaque characterization by magnetic resonance imaging: review of the literature. Top Magn Reson Imaging 2001;12:205–217.
5. Ying L, Liang ZP. Parallel MRI using phased array coils. IEEE Signal Process Mag 2010;27:90–98.
6. Lustig M, Donoho DL, Pauly JM. Sparse MRI: the application of compressed sensing for rapid MR imaging. Magn Reson Med 2007;58:1182–1195.
7. Liang ZP. Spatiotemporal imaging with partially separable functions. Proc IEEE Int Symp Biomed Imaging 2007:988–991.
8. Griswold MA, Jakob PM, Heidemann RM, Nittka M, Jellus V, Wang J, Kiefer B, Haase A. Generalized autocalibrating partially parallel acquisitions (GRAPPA). Magn Reson Med 2002;47:1202–1210.
9. Pruessmann KP, Weiger M, Scheidegger MB, Boesiger P. SENSE: sensitivity encoding for fast MRI. Magn Reson Med 1999;42:952–962.
10. Lustig M, Pauly JM. SPIRiT: iterative self-consistent parallel imaging reconstruction from arbitrary k-space. Magn Reson Med 2010;64:457–471.
11. Feng L, Otazo R, Jung H, Jensen JH, Ye JC, Sodickson DK, Kim D. Accelerated cardiac T2 mapping using breath-hold multiecho fast spin-echo pulse sequence with k-t FOCUSS. Magn Reson Med 2011; 65:1661–1669.
12. Majumdar A, Ward RK. Accelerating multi-echo T2 weighted MR imaging: analysis prior group-sparse optimization. J Magn Reson Imaging 2011;210:90–97.
13. Velikina JV, Alexander AL, Samsonov A. Accelerating MR parameter mapping using sparsity-promoting regularization in parametric dimension. Magn Reson Med 2013;70:1263–1273.
14. Petzschner FH, Ponce IP, Blaimer M, Jakob PM, Breuer FA. Fast MR parameter mapping using k-t principal component analysis. Magn Reson Med 2011;66:706–716.
15. Huang C, Graff CG, Clarkson EW, Bilgin A, Altbach MI. T2 mapping from highly undersampled data by reconstruction of principal component coefficient maps using compressed sensing. Magn Reson Med 2012;67:1355–1366.
16. Zhao B, Lu W, Liang ZP. Highly accelerated parameter mapping with joint partial separability and sparsity constraints. In Proceedings of the 20th Annual Meeting of ISMRM, Melbourne, Australia, 2012. Abstract 2233.
17. Zhao B, Lu W, Hitchens TK, Lam F, Ho C, Liang ZP. Accelerated MR parameter mapping with low-rank and sparsity constraints. Magn Reson Med 2015;74:489–498.
18. Doneva M, Sénégas J, Börnert P, Eggers H, Mertins A. Accelerated MR parameter mapping using compressed sensing with model-based sparsifying transform. In Proceedings of the 17th Annual Meeting of ISMRM, Honolulu, Hawaii, USA, 2009. Abstract 2812.
19. Doneva M, Bornert P, Eggers H, Stehning C, Sngas J, Mertins A. Compressed sensing reconstruction for magnetic resonance parameter mapping. Magn Reson Med 2010;64:1114–1120.

20. Sénégas J, Liu W, Dahnke H, Song H, Jordan EK, Frank JA. Fast T2 relaxometry with accelerated multi-echo spin echo sequence. NMR Biomed 2010;23:958–967.
21. Cadzow JA. Signal enhancement - a composite property mapping algorithm. IEEE Trans Acoust Speech Sign 1988;36:49–62.
22. Nguyen HM, Peng X, Do MN, Liang ZP. Denoising MR spectroscopic imaging data with low-rank approximations. IEEE Trans Biomed Eng 2013;60:78–89.
23. Wu Y, Zhu Y, Tang Q, Liu W, Dai R, Liu X, Wu X, Ying L, Liang D. Accelerated MR diffusion tensor imaging using distributed compressed sensing. Magn Reson Med 2014;71:763–772.
24. Eliezer N, Sodickson DK, Block KT. Rapid and accurate T2 mapping from multi–spin-echo data using Bloch-simulation-based reconstruction. Magn Reson Med 2015;73:809–817.
25. Boogaart A, Ormondt D, Pijnappel WWF, Beer R, Korpela M. Removal of the water resonance from 1H magnetic resonance spectra. In: McWhirter JG, editor. Mathematical signal processing III. London, UK: Oxford, Clarendon Press; 1994. p 175–195.
26. Pijnappel WWF, Boogaart A, Beer R, Ormondt D. SVD-based quantification of magnetic resonance signals. J Magn Reson 1992;97:122–134.
27. Montefusco LB, Lazzaro D, Papi S. Nonlinear filtering for sparse signal recovery from incomplete measurements. IEEE Trans Sig Process 2009;57:2494–2502.
28. Gould NIM. On the convergence of a sequential penalty function method for constrained minimization. SIAM J Numer Anal 1989;26: 107–128.
29. Pruessmann KP, Weiger M, Bornert P, Boesiger P. Advances in sensitivity encoding with arbitrary k-space trajectories. Magn Reson Med 2011;46:638–651.
30. Collins DL, Zijdenbos AP, Kollokian V, Sled JG, Kabani NJ, Holmes CJ, Evans AC. Design and construction of a realistic digital brain phantom. IEEE Trans Med Imaging 1998;17:463–468.
31. Griffiths DJ. Introduction to electrodynamics. 3rd edition. Boston: Addison Wesley; 1999.
32. Walsh DO, Gmitor AF, Marcellin MW. Adaptive reconstruction of phased array MR imagery. Magn Reson Med 2000;43:682–690.
33. Haldar JP, Hernando D, Liang ZP. Super-resolution reconstruction of MR image sequences with contrast modeling. Proc IEEE Int Symp Biomed Imaging 2009:266–269.
34. Block K, Uecker M, Frahm J. Model-based iterative reconstruction for radial fast spin-echo MRI. IEEE Trans Med Imaging 2009;28:1759–1769.
35. Sumpf TJ, Uecker M, Boretius S, Frahm J. Model-based nonlinear inverse reconstruction for mapping using highly undersampled spin-echo MRI. J Magn Reson Imaging 2011;34:420–428.
36. Zhao B, Lam F, Liang ZP. Model-based MR parameter mapping with sparsity constraints: parameter estimation and performance bounds. IEEE Trans Med Imaging 2014;33:1832–1844.
37. Peng X, Liu X, Zheng H, Liang D. Exploiting parameter sparsity in model-based reconstruction to accelerate proton density and T2 mapping. Med Eng Phys 2014;36:1428–1435.
38. Zhu Y, Wu Y, Wu EX, Ying L, Liang D. A model-based method with joint sparsity constraint for direct diffusion tensor estimation. Proc IEEE Int Symp Biomed Imaging 2012:510–513.
39. Welsh CL, DiBella EVR, Adluru G, Hsu EW. Model-based reconstruction of undersampled diffusion tensor k-space data. Magn Reson Med 2013;70:429–440.
40. Peng X, Ying L, Liu X, Liang D. Accurate T2 mapping with sparsity and linear predictability filtering. Proc IEEE Int Symp Biomed Imaging 2014:161–164.
41. Shi C, Zhou Y, Wang Y, Lyu J, Liang D, Ying L. Recovery of parametric manifold from reduced measurements: application to magnetic resonance parameter mapping. Proc IEEE Int Symp Biomed Imaging 2015:901–904.
42. Zhu Y, Zhang Q, Liu Q, Wang Y, Liu X, Zheng H, Liang D, Yuan J. PANDA-T1rho: integrating principal component analysis and dictionary learning for fast T1rho mapping. Magn Reson Med 2014;73: 263–272.